HHS Public Access

Author manuscript

J Biomech. Author manuscript; available in PMC 2017 June 14.

Published in final edited form as:

J Biomech. 2016 June 14; 49(9): 1562–1569. doi:10.1016/j.jbiomech.2016.03.034.

A Structural Finite Element Model for Lamellar Unit of Aortic Media Indicates Heterogeneous Stress Field After Collagen Recruitment

James R. Thunes[1], **Siladitya Pal**[6], **Ronald N. Fortunato**[1], **Julie A. Phillippi**[1,2,3,4,5], **Thomas G. Gleason**[1,2,3,4,5], **David A. Vorp**[1,2,3,4,5], and **Spandan Maiti**[1,*]

[1]Department of Bioengineering, University of Pittsburgh, Pittsburgh, PA, United States

[2]Cardiothoracic Surgery, University of Pittsburgh, Pittsburgh, PA, United States

[3]Surgery, University of Pittsburgh, Pittsburgh, PA, United States

[4]Center for Vascular Remodeling and Regeneration, University of Pittsburgh, Pittsburgh, PA, United States

[5]McGowan Institute for Regenerative Medicine, University of Pittsburgh, Pittsburgh, PA, United States

[6]Mechanical and Industrial Engineering Department, Indian Institute of Technology Roorkee, Roorkee, India

Abstract

Incorporation of collagen structural information into the study of biomechanical behavior of ascending thoracic aortic (ATA) wall tissue should provide better insight into the pathophysiology of ATA. Structurally motivated constitutive models that include fiber dispersion and recruitment can successfully capture overall mechanical response of the arterial wall tissue. However, these models cannot examine local microarchitectural features of the collagen network, such as the effect of fiber disruptions and interaction between fibrous and non-fibrous components, which may influence emergent biomechanical properties of the tissue. Motivated by this need, we developed a finite element based three-dimensional structural model of the lamellar units of the ATA media that directly incorporates the collagen fiber microarchitecture. The fiber architecture was computer generated utilizing network features, namely fiber orientation distribution, intersection density and areal concentration, obtained from image analysis of multiphoton microscopy images taken from human aneurysmal ascending thoracic aortic media specimens with bicuspid aortic valve (BAV) phenotype. Our model reproduces the typical J-shaped constitutive response of the aortic wall tissue. We found that the stress state in the non-fibrous matrix was homogeneous until the collagen fibers were recruited, but became highly heterogeneous after that event. The degree of heterogeneity was dependent upon local network architecture with high

*Corresponding author: ; Email: spm54@pitt.edu, Telephone: 412-624-4240, Fax: 412-383-8788

stresses observed near disrupted fibers. The magnitude of non-fibrous matrix stress at higher stretch levels was negatively correlated with local fiber density. The localized stress concentrations, elucidated by this model, may be a factor in the degenerative changes in aneurysmal ATA tissue.

1 Introduction

Biomechanical response of the ascending thoracic aortic (ATA) wall tissue plays an important role in the pathophysiology of the thoracic aorta. Primary load-bearing components of the ATA media are lamellar units (LU) consisting of elastic lamellae encompassing vascular smooth muscle cells (VSMC), interposed with collagen fiber network (Figure 1b). Incorporation of the above mentioned structural features of the lamellar units are thus essential in the study of biomechanical response of ATA wall tissue. A number of structurally motivated constitutive models for the arterial wall have recently appeared in the literature that augment the strain energy expression with additional terms incorporating experimentally observed collagen fiber tortuosity and orientation (Ferruzzi et al., 2011; Gasser et al., 2006; Holzapfel et al., 2004; Wan et al., 2012; Weisbecker et al., 2015; Zulliger and Stergiopulos, 2007). These constitutive models are a major improvement over purely phenomenological models, and are quite successful in fitting the overall stress-strain response of arterial wall tissue specimens. However, these models are not fully structural representations of the aortic wall. Thus they cannot examine, for example, the effect of physiological fiber network architecture and fiber-nonfibrous matrix interaction on the biomechanical state of the wall tissue. These lamellar scale details can give rise to locally heterogeneous stress distribution within the elastic lamellae and may influence structural and functional remodeling of the extracellular matrix by the VSMCs mediated by local mechanical stimuli.

Our goal in this study was to develop a finite element based modeling framework leading towards true structural representation of the ATA media lamellar unit. To achieve this goal, we developed a novel fiber reinforced finite element method capable of embedding 1D fibers of arbitrary orientation within 3D finite elements. Using this framework, we created a representation of the lamellar unit of the human aortic media that directly included structural features of the tissue. The developed model could recapitulate the uniaxial constitutive response of the media successfully. Additionally, our model revealed that stress state in the non-collagenous matrix is homogeneous at low stretch, but becomes highly heterogeneous at higher stretch levels after collagen fiber recruitment. Magnitude of non-collagenous matrix stress depends on the local architecture of the collagen network. Further, collagen fibers oriented themselves in the loading direction, and created distinct “stress paths” that were the primary load-bearing mechanism at high stretch.

2 Methods

2.1 Computational domain and finite element simulation methodology

We constructed a 3D representative volume element (RVE) to simulate the biomechanical response of a single LU within the ATA media (Figure 1c). Thickness of the elastic lamellae

and spacing between them vary radially within the media. Depth-averaged values of these parameters, namely lamella thickness of 1.5 μm and interlamellar (IL) spacing of 11 μm were thus chosen (O'Connell et al., 2008). We exploited lamellar unit symmetry in the radial (RAD) direction by modeling only half of it. A network of 21,000 elastin fibers was embedded within the domain to represent the elastin lamella. The volume fraction of elastin within the lamella was 85% (10% of total RVE volume). Elastin fiber orientation was taken from previously reported data (normalized orientation index (NOI) 0.70) (Phillippi et al., 2014). As planar dispersion of collagen fibers was more significant than out-of-plane components (Holzapfel et al., 2015), our computer-generated collagen fiber network (Figure 1e) resided solely on CIRC-LONG plane and was embedded within the 3D interlamellar space just below the elastic lamella. CIRC and LONG dimensions of the computational domain were both 250 μm, in accordance with the multiphoton microscopy (MPM) image dimensions from which the fiber network was constructed. As there is a depth-wise variation of fiber network within the media, we did not use fiber arrangement derived from a single MPM image. Instead, we averaged network features of interest from the images taken over depth of the media at an increment of 10 μm (Koch et al., 2014). Fiber microarchitecture was computer generated using these average features. Similar image-based computational representations of fiber networks were recently reported in the context of electrospun polymeric materials (Carleton et al., 2015; D'Amore et al., 2014). The orientation distribution (OD) reported in (Phillippi et al., 2014) and fiber intersection density and areal concentration reported in (Koch et al., 2014) were used as inputs for the construction of our computational fiber network (Figure 1e). Network construction was performed by first creating a Voronoi tessellation and then modifying it systematically to achieve target values of all input parameters (Figure S1). The bin-by-bin fit of the orientation distribution (OD) between the image-derived and simulated networks (Figure 2) was quantified using a two-sample chi-squared test ($p \leq 0.05$ denoting equivalence). Values of other input parameters for the network creation are shown in Table 1. The resulting volume fraction of collagen fibers was 16%. To determine the effect of the collagen network architecture on the tissue response, five networks each for BAV and TAV (tricuspid aortic valve) ATA specimens were created using the mean and standard error of NOI reported in (Phillippi et al., 2014), keeping other network parameters (listed in Table 1) constant. The interlaminar space, consisting of VSMCs, ground substance etc., was collectively referred as the interlaminar non-fibrous matrix.

The RVE was discretized with custom-developed fiber-embedded finite elements representing collagen or elastin fiber segments (Figure 3a) and 8-noded hexahedral elements. Kinematically constrained “virtual nodes” at the end of bar elements enabled them to interact with the hexahedral elements. Affine deformation of the fiber and the surrounding non-fibrous matrix was assumed so that isoparametric coordinates of the virtual nodes in relation to the parent hexahedral element remained constant throughout the simulations. A line-plane intersection search algorithm (O'Rourke, 1998) was employed to identify the virtual nodes on the faces of the solid element. Details of the finite element formulation are given in the supplementary information.

The RVE was subjected to an applied stretch of λ=1.5 in CIRC direction on the LONG-RAD face while all other faces, except the upper face that was kept free, were on rollers. This set

of boundary conditions ensured a homogeneous strain field within the RVE in the absence of collagen fibers. Finite element simulations were performed using a custom nonlinear finite element code previously developed and applied to various biomechanical studies (Pal et al., 2014; Thunes et al., 2015). Convergence analysis of the simulated stress-stretch response suggested a mesh of 10,800 8-noded hexahedral elements with the stretch applied over 400 steps was sufficient to yield converged results. Stress contours were plotted using Paraview 4.1.0 (Ahrens et al., 2005). The means of the non-fibrous matrix stresses between the fiber stretches at different applied stretch levels was compared using a paired t-test while differences between the variance for those data were computed using Levene's test (Matlab 2014b, Mathworks, Natick, MA). A paired t-test was used to determine differences between maximum non-fibrous matrix stresses of the BAV and TAV specimens.

2.2 Constitutive model and parameter identification

Collagen fibers were assumed not to take any load in compression, while a bilinear constitutive response was assumed in tension:

$$\sigma = \begin{cases} 0 & \text{if } \lambda < \lambda_r \\ E_f(\lambda - \lambda_r) & \text{if } \lambda \geq \lambda_r \end{cases}$$

with λ as fiber stretch, λ_r as recruitment stretch, and E_f is the elastic modulus of the fiber, respectively (Figure 3b). All collagen fibers were modeled with 3 μm diameter (Koch et al., 2014), while that for elastin fibers was 0.1 μm diameter (Shah et al., 2014). Non-fibrous matrix was modeled as one parameter isotropic incompressible neo-Hookean material (Weisbecker et al., 2013) with the strain energy function:

$$\Psi = \frac{\mu}{2}(I_1 - 3)$$

where μ and I_1 are shear modulus and the first invariant of the right Cauchy-Green deformation tensor, respectively. As shear modulus for elastin lies in the range of 100–1000 kPa (Fung, 1993), E_f for the elastin fibers was taken to be 3 MPa. Simulated constitutive response of the tissue was regressed against the experimental curves previously obtained from experimentally dissected intimal half of aneurysmal aortic tissue of patients with BAV, and reported in (Pasta et al., 2013) to find values for the remaining three material parameters: μ_M (shear modulus of non-fibrous matrix), E_f, and λ_r (Table 2). These parameters were used for the simulations with the other aneurysmal BAV and TAV collagen networks. Goodness-of-fit between the experimental and simulated stress-stretch response was determined using the coefficient of determination (R^2), and a good correlation (R^2 = 0.996) was obtained, Figure 4.

3 Results

3.1 Stress distribution in the interlaminar non-fibrous matrix

The CIRC component of Cauchy stress tensor in the IL region on the CIRC-LONG plane in the immediate vicinity of the collagen network at different applied stretches is presented in

Figure 5. The fiber network was superimposed in white in all panels to reveal the features of the non-fibrous matrix stress distribution in relation to the spatial arrangement of collagen fibers. Figure 5 demonstrates that the stress state in the non-fibrous matrix was homogeneous up to recruitment stretch of the collagen fibers ($\lambda = 1.25$). However, the non-fibrous matrix stress distribution started to exhibit local perturbations once the applied stretch exceeded λ_r. Average CIRC stress at $\lambda = 1.35$ was 210 kPa, while the maximum and minimum stress values are 550 and −60 kPa, respectively. Additionally, we noted that stress peaks localized to regions where collagen fibers appeared discontinuous in CIRC direction (Figure 5). A stretch of 1.5 accentuated this pattern of increased non-fibrous matrix stress in areas of focal disruption of collagen. To wit, maximum non-fibrous matrix stress at this stretch was 1.8 MPa and the minimum stress was −0.42 MPa. Similar trends were seen with the aneurysmal TAV tissue (Figure 5 lower panels). However, stress peaks were lower in number and magnitude at $\lambda=1.5$ for TAV tissue compared to the BAV tissue.

To further examine the evolution of IL non-fibrous matrix stress heterogeneity with applied stretch, CIRC stress components at all Gauss points within the IL non-fibrous matrix were collected, and the resulting stress distribution at four levels of applied stretch are shown in Figure 6. A positive correlation of the mean IL non-fibrous matrix stress with the applied stretch was observed ($p < 0.01$, Figure 6). Standard deviation of CIRC stress was consistently less than 10 kPa until $\lambda=1.25$, the recruitment stretch, while it increased dramatically beyond this stretch. The coefficient of variance in the non-fibrous matrix stress increased from 0.1 before λ_r to 1.25 at $\lambda=1.5$. Levene's test showed that the standard deviations of the stress below $\lambda=1.25$ were similar to one another ($p > 0.05$) but varied above $\lambda=1.25$ ($p < 0.01$).

3.2 Fiber reorientation and recruitment with applied stretch

To examine the effect of applied stretch on fiber recruitment and reorientation, we monitored the stress state of each fiber segment at all increments of applied stretch. Lengths of all fiber segments subjected to tensile loading at a given λ were added together, and then was divided by the length of the entire fiber network to obtain the load-bearing fraction of the network. A plot of this fraction, expressed in percentage, reveals that none of the collagen fibers were loaded up to the recruitment stretch, $\lambda=1.25$ (Figure 7). Beyond the point of recruitment stretch, not all the fibers started to bear load simultaneously; this intermediary event occurred between $\lambda=1.25$ to approximately $\lambda=1.4$. At the end of the recruitment period, 90% of the total length of the fibers in the network was subjected to tensile loading. It is interesting to note that all fiber segments were not subjected to loading even at high applied stretch of 1.5.

To study remodeling of the fiber network in aortic tissue under applied stretch, we computed the orientation of all fiber segments at each applied stretch level with fiber angle data gathered in 0.5° increments and fit to a normal distribution function. While most fibers in the network aligned with the loading direction to some extent, the degree to which they reoriented depended on the initial orientation of each fiber as well as the magnitude of applied stretch. Inspection of the orientation distribution functions (ODF) of the network at five stretch levels, along with the actual network topology reveal that fiber reorientation

began immediately at the onset of loading, even though fibers were not bearing any load below the recruitment stretch (Figure 8). Mean fiber orientation (CIRC direction) was maintained during applied stretch in the CIRC direction, and became more uniform as evidenced by the noted reduction in standard deviation with increasing applied stretch (Levene's test $p < 0.01$ for all combinations). NOI (D'Amore et al., 2010), a measure of network alignment, increased from 56% under no load to 62% at λ=1.5, where 0% denotes a totally isotropic and 100% a fully aligned network. Change of orientation for individual fiber segments depended on their orientation from the loading (CIRC) direction in the reference configuration. For example, the mean change in angle for fibers oriented between 30–60° was 9°, while that for fibers oriented between 70–90° was 1°.

3.3 Stress in the fiber network

Of particular importance, this model revealed a striking association between decreased fiber density and increased stress state within the non-fibrous matrix (Figure 9). For low applied stretches up to λ_f, the fibers did not experience any loading. However, at higher stretch levels (λ=1.35 and 1.5 in Figure 9), the collagen fibers started to experience tensile stress. We observed that magnitude of fiber stress was heterogeneous. Segments aligned with the loading direction (CIRC) experienced maximum stress, while longitudinally oriented fibers did not participate in any load bearing. Further, some fiber segments were found to follow continuous "stress paths" percolating between the loading ends, an outcome of local network microarchitectural features combined with gradual reorientation. (Zagar et al., 2015) recently demonstrated formation of such "stress paths" in the large strain response of biopolymer networks. They also suggested reorientation of these stress paths as a fundamental mechanism of stiffening in stretch-dominated networks. We additionally found that regions of fiber disruption along CIRC direction, for example those marked with white arrows, was strikingly associated with focal regions of high stress in the non-fibrous matrix (lighter background color). The non-fibrous matrix stress in regions of fiber disruption varied between 0.8 and 1.8 MPa while the fiber stresses were between 8 and 10 MPa at λ=1.5. To investigate the relationship between local fiber architecture and non-fibrous matrix stress at higher applied stretches further, we considered all 3D finite elements intersected by fiber network plane. We calculated the "local fiber density" by dividing the total volume of fiber segments contained in each finite element by the volume of the 3D element itself. CIRC stresses calculated at all eight Gauss points in an element were averaged element-wise, and were plotted against local fiber density in Figure 10 for λ=1.5. We observed a weak negative correlation (R=0.2, $p < 0.05$) that revealed decreased local fiber density to be associated with high non-fibrous matrix stress state.

4 Discussion

4.1 Structural model of lamellar unit of aortic media recapitulates its constitutive behavior

Elastic lamellar units, the primary load-bearing structure of human ATA media, are arranged radially in a repetitive fashion in 40–60 layers (Benninghoff, 1928). Accordingly, we modeled a portion of the LU as the representative volume element of the aortic media (Figure 1). A representative collagen fiber network, constructed using empirically derived fiber network features from multi-photon microscopy, was directly incorporated in the RVE.

Network features in addition to orientation distribution such as fiber intersection density, areal density, and average segment length can have a significant influence on network mechanics (Carleton et al., 2015; Picu, 2011). Our computational approach included all these network parameters, and also allowed for fiber-non-fibrous matrix interaction by the way of novel fiber-embedded finite element technique. Resulting model revealed heterogeneous non-fibrous matrix stress field in the human aortic media at higher applied stretch. Our approach is unique and in contrast with current structurally motivated models for the aortic wall, where an anisotropic and homogeneous media is assumed. Direct embedment of fibers within the non-fibrous matrix has been previously considered by (Zhang et al., 2013a; Zhang et al., 2013b) in the general context of fiber reinforced soft tissue mechanics. However, in these works, the fibers were restricted to align with the edges of the finite elements making mesh generation a non-trivial task for large number of fibers. In contrast, our method incorporates multiple fibers in arbitrary orientation within a solid element thus rendering volumetric meshing a simple task. Our model correctly predicted the nearly linear elastin-dominated low stretch regimen as well as the linear collagen-dominated high stretch regimen. Gradual recruitment of collagen fibers, as predicted by our model, gave rise to nonlinearity of the response curve joining these linear portions (Figure 4).

4.2 Stress field in interlaminar matrix becomes heterogeneous after collagen fiber recruitment

We also show that the non-fibrous matrix stress became heterogeneous once collagen fibers started to transmit load, heterogeneities being markedly accentuated at higher stretch levels (Figure 5). Interestingly, the magnitude of stress heterogeneities differed between the simulated BAV and TAV ATA specimens. For example, at λ=1.4, peak CIRC stress for BAV ATA specimens (660 KPa) was significantly different ($p=0.047$) than that for TAV ATA (590 KPa) suggesting that difference in collagen microarchitecture between heart valve phenotypes may be an important factor influencing localized variations in the interlaminar stress field. The stress level in the collagen fibers also varied substantially, with fibers oriented in the loading direction carrying more stress (Figure 9). Fiber stress is concentrated on a small number of stress paths for the BAV ATA network while the stress is distributed among a majority of the aligned fibers in the TAV network. Additionally, fiber segments oriented within 70° of the loading direction continually reoriented thus altering the distribution of stress in the fiber network. Matrix stress heterogeneity is an outcome of local fiber network microarchitecture (e.g. density) as well as fiber-matrix interaction. Due to the assumption of perfect bonding between the fibers and the non-fibrous matrix, they deformed in an affine manner, a reasonable assumption for soft tissue mechanics (Lake et al., 2012). In presence of recruited fibers, matrix in the vicinity attempts to match fiber strain to maintain perfect bonding between them. Collagen fibers experience a higher stress and effectively shield the matrix because the collagen elastic modulus is at least an order of magnitude higher than the modulus for matrix (Fung, 1993). However, it can be noted from qualitative inspection of matrix stress “heat maps” overlayed with fiber network images that wherever the fibers are discontinuous in the loading (CIRC) direction, the intervening matrix stress is focally elevated in an attempt to match the stress state of the fibers in the vicinity (Figure 9). The correlation between decreased local fiber density and increased interlaminar matrix stress in the vicinity (Figure 10) raises the question of the potential for delamination in these

regions. We noted that the stress heterogeneities manifested beyond the physiological range of wall stretch (~1.2). Therefore, these findings might be more likely in the setting of altered collagen microarchitecture in hypertensive patients. Locally elevated stress can adversely affect the biology of the aortic wall as VSMCs are mechanosensitive (Haga et al., 2007) and stress state can alter their phenotype (Acampora et al., 2010). The impact of VSMC-matrix interactions on local stress will require further investigation. Taken together with recent work from our group and others (Forsell et al., 2014; Phillippi et al., 2014; Pichamuthu et al., 2013; Sokolis et al., 2012) these results indicate a role for collagen network microarchitecture architecture in aortic wall biomechanics.

4.3 Limitations of current modeling approach

Our computational model for the human thoracic aortic media has some limitations. We assumed the interlaminar matrix to be homogeneous to act as a single material in our model. The multi-component nature of the IL space along with contractile forces from the VSMCs can alter the stress state of aortic media. However, heterogeneities in the IL matrix material are expected to contribute to fluctuations in the stress field, and thus our basic conclusions will likely not change. Furthermore, we did not consider mechanical failure of any of the model components. Our model predicted markedly high stresses which could lead to failure of the fiber matrix and hence, alteration of stress distribution. Finally, we have considered only uniaxial stretching of the aortic media. It will be interesting to examine whether our model can capture constitutive responses under multiaxial loading, which is a topic of our future research.

5 Conclusions

We have presented a finite element structural model of the aortic media considering its lamellar architecture. An important aspect of our approach is the use of only experimentally-derived information as model parameters. The model correctly reproduced nonlinear mechanical response of the wall tissue and importantly, revealed a heterogeneity in the stress state of fibers and matrix throughout the entire stretching event. We found that fiber-matrix interaction, combined with local fiber microarchitecture, gave rise to heterogeneous stress field within the aortic media after the fibers started taking load. Fluctuations in the interlaminar matrix stress continually increased with applied stretch, creating regions of higher stress that local VSMCs could experience. We expect that our computational approach will provide insight into the role of structural changes of the aortic wall and ensuing wall tissue biomechanical response on the pathophysiology of aortic disease, such as aneurysm and dissection, and contribute metrics from non-invasive clinical imaging data to help guide clinical decision-making and care of patients with aortic disease.

Supplementary Material

Refer to Web version on PubMed Central for supplementary material.

Acknowledgments

Support for J. Thunes was provided by an NPSC fellowship.

Conflict of Interest

The authors do not have any financial interest or other relationship (grant, research support, consultant, etc.) with any manufacturer(s) of any commercial product(s) to disclose.

References

Acampora KB, Nagatomi J, Langan EM 3rd, LaBerge M. Increased synthetic phenotype behavior of smooth muscle cells in response to in vitro balloon angioplasty injury model. Ann Vasc Surg. 2010; 24:116–126. [PubMed: 19781909]

Ahrens, James; Geveci, Berk; Law, Charles. ParaView: An End-User Tool for Large Data Visualization. Elsevier; 2005.

Benninghoff A. Uber die Beziehungen zwischen elastischen Gerust und glatter Muskulatur in der Arterienwand und ihre funktionelle Bedeutung. Z. Zellforsch. Mikroskop. Anat. Abt. Histochem. 1928; 6:348.

Carleton JB, D'Amore A, Feaver KR, Rodin GJ, Sacks MS. Geometric characterization and simulation of planar layered elastomeric fibrous biomaterials. Acta Biomater. 2015; 12:93–101. [PubMed: 25311685]

D'Amore A, Amoroso N, Gottardi R, Hobson C, Carruthers C, Watkins S, Wagner WR, Sacks MS. From single fiber to macro-level mechanics: A structural finite-element model for elastomeric fibrous biomaterials. Journal of the mechanical behavior of biomedical materials. 2014; 39:146–161. [PubMed: 25128869]

D'Amore A, Stella JA, Wagner WR, Sacks MS. Characterization of the complete fiber network topology of planar fibrous tissues and scaffolds. Biomaterials. 2010; 31:5345–5354. [PubMed: 20398930]

Ferruzzi J, Vorp DA, Humphrey JD. On constitutive descriptors of the biaxial mechanical behaviour of human abdominal aorta and aneurysms. J R Soc Interface. 2011; 8:435–450. [PubMed: 20659928]

Forsell C, Bjorck HM, Eriksson P, Franco-Cereceda A, Gasser TC. Biomechanical properties of the thoracic aneurysmal wall: differences between bicuspid aortic valve and tricuspid aortic valve patients. Ann Thorac Surg. 2014; 98:65–71. [PubMed: 24881863]

Fung, YC. Biomechanics: Mechanical Properties of Living Tissue. 2. New York: Springer-Verlag; 1993.

Gasser TC, Ogden RW, Holzapfel GA. Hyperelastic modelling of arterial layers with distributed collagen fibre orientations. J R Soc Interface. 2006; 3:15–35. [PubMed: 16849214]

Haga JH, Li YS, Chien S. Molecular basis of the effects of mechanical stretch on vascular smooth muscle cells. J Biomech. 2007; 40:947–960. [PubMed: 16867303]

Holzapfel GA, Gasser TC, Ogden RW. Comparison of a Multi-Layer Structural Model for Arterial Walls With a Fung-Type Model, and Issues of Material Stability. Journal of Biomechanical Engineering. 2004; 126:264. [PubMed: 15179858]

Holzapfel GA, Niestrawska JA, Ogden RW, Reinisch AJ, Schriefl AJ. Modelling non-symmetric collagen fibre dispersion in arterial walls. J R Soc Interface. 2015; 12

Koch RG, Tsamis A, D'Amore A, Wagner WR, Watkins SC, Gleason TG, Vorp DA. A custom image-based analysis tool for quantifying elastin and collagen micro-architecture in the wall of the human aorta from multi-photon microscopy. J Biomech. 2014; 47:935–943. [PubMed: 24524988]

Lake SP, Hadi MF, Lai VK, Barocas VH. Mechanics of a fiber network within a non-fibrillar matrix: model and comparison with collagen-agarose co-gels. Ann Biomed Eng. 2012; 40:2111–2121. [PubMed: 22565816]

O'Connell MK, Murthy S, Phan S, Xu C, Buchanan J, Spilker R, Dalman RL, Zarins CK, Denk W, Taylor CA. The three-dimensional micro- and nanostructure of the aortic medial lamellar unit measured using 3D confocal and electron microscopy imaging. Matrix Biol. 2008; 27:171–181. [PubMed: 18248974]

O'Rourke, J. Computational Geometry in C. 2. Cambridge University Press; 1998.

Pal S, Tsamis A, Pasta S, D'Amore A, Gleason TG, Vorp DA, Maiti S. A mechanistic model on the role of "radially-running" collagen fibers on dissection properties of human ascending thoracic aorta. J Biomech. 2014; 47:981–988. [PubMed: 24484644]

Pasta S, Rinaudo A, Luca A, Pilato M, Scardulla C, Gleason TG, Vorp DA. Difference in hemodynamic and wall stress of ascending thoracic aortic aneurysms with bicuspid and tricuspid aortic valve. J Biomech. 2013; 46:1729–1738. [PubMed: 23664314]

Phillippi JA, Green BR, Eskay MA, Kotlarczyk MP, Hill MR, Robertson AM, Watkins SC, Vorp DA, Gleason TG. Mechanism of aortic medial matrix remodeling is distinct in patients with bicuspid aortic valve. J Thorac Cardiovasc Surg. 2014; 147:1056–1064. [PubMed: 23764410]

Pichamuthu JE, Phillippi JA, Cleary DA, Chew DW, Hempel J, Vorp DA, Gleason TG. Differential tensile strength and collagen composition in ascending aortic aneurysms by aortic valve phenotype. Ann Thorac Surg. 2013; 96:2147–2154. [PubMed: 24021768]

Picu RC. Mechanics of random fiber networks—a review. Soft Matter. 2011; 7:6768.

Shah SB, Witzenburg C, Hadi MF, Wagner HP, Goodrich JM, Alford PW, Barocas VH. Prefailure and failure mechanics of the porcine ascending thoracic aorta: experiments and a multiscale model. J Biomech Eng. 2014; 136:021028. [PubMed: 24402447]

Sokolis DP, Kritharis EP, Giagini AT, Lampropoulos KM, Papadodima SA, Iliopoulos DC. Biomechanical response of ascending thoracic aortic aneurysms: association with structural remodelling. Computer methods in biomechanics and biomedical engineering. 2012; 15:231–248. [PubMed: 21480082]

Thunes J, Matthew Miller R, Pal S, Damle S, Debski RE, Maiti S. The Effect of Size and Location of Tears in the Supraspinatus Tendon on Potential Tear Propagation. J Biomech Eng. 2015; 137:081012. [PubMed: 26043431]

Wan W, Dixon JB, Gleason RL Jr. Constitutive modeling of mouse carotid arteries using experimentally measured microstructural parameters. Biophysical journal. 2012; 102:2916–2925. [PubMed: 22735542]

Weisbecker H, Unterberger MJ, Holzapfel GA. Constitutive modelling of arteries considering fibre recruitment and three-dimensional fibre distribution. J R Soc Interface. 2015; 12

Weisbecker H, Viertler C, Pierce DM, Holzapfel GA. The role of elastin and collagen in the softening behavior of the human thoracic aortic media. J Biomech. 2013; 46:1859–1865. [PubMed: 23735660]

Zagar G, Onck PR, van der Giessen E. Two fundamental mechanisms govern the stiffening of cross-linked networks. Biophys J. 2015; 108:1470–1479. [PubMed: 25809259]

Zhang L, Lake SP, Barocas VH, Shephard MS, Picu RC. Cross-Linked Fiber Network Embedded in Elastic Matrix. Soft Matter. 2013a; 9:6398–6405. [PubMed: 24089623]

Zhang L, Lake SP, Lai VK, Picu CR, Barocas VH, Shephard MS. A coupled fiber-matrix model demonstrates highly inhomogeneous microstructural interactions in soft tissues under tensile load. J Biomech Eng. 2013b; 135:011008. [PubMed: 23363219]

Zulliger MA, Stergiopulos N. Structural strain energy function applied to the ageing of the human aorta. J Biomech. 2007; 40:3061–3069. [PubMed: 17822709]

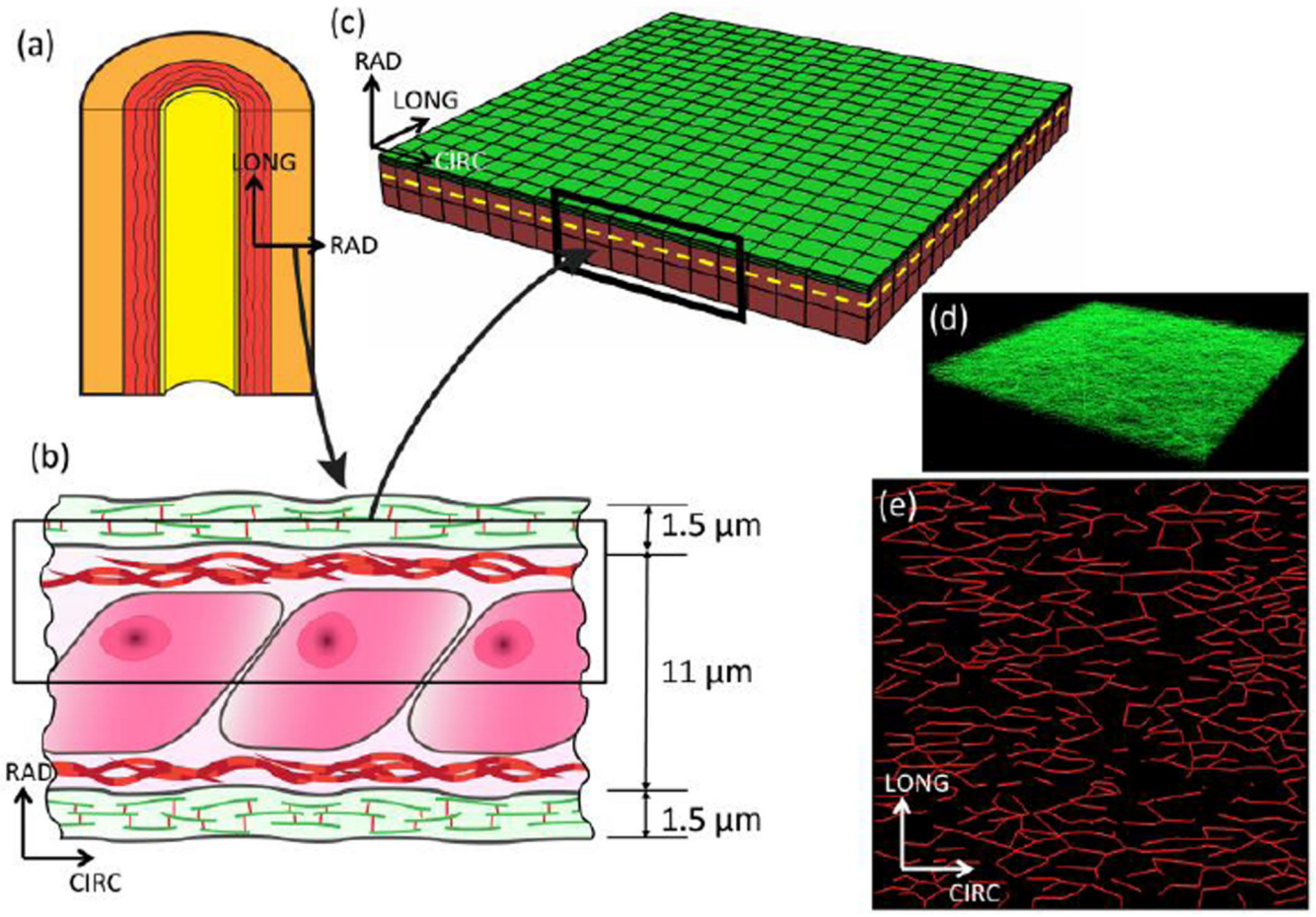

Figure 1.

The aorta (a) is composed of three layers: the intima (yellow region), media (red region), and adventitia (orange region). The media is composed of multiple layers of elastin separated by interlaminar space. The lamellar unit of the aortic media (b) was used to create a representative volume element for the finite element simulation (c). The RVE dimensions were taken as 250 × 250 × 6.25 μm. The green region represents an elastic lamella while the red region represents the interlaminar space. For the simulation, the constituents of the IL space: cells, glycosaminoglycans, etc. have been homogenized to an isotropic material. Only half of the lamellar unit (shown by black rectangle in (b)) has been modeled considering its symmetry. To highlight the mesh discretization, a 75 × 75 × 6.25 μm section of the mesh is shown. The elastic lamella is represented in the model by a network of elastin fibers. This network (d) is composed of 21,000 fiber segments. A representative (10 × 10 × 0.75 μm) portion of the elastic lamella has been plotted to show the dense 3D nature of the network. The collagen network (e) (shown in (c) by the dotted yellow line) is situated directly below the elastin network and is composed of 860 fiber segments.

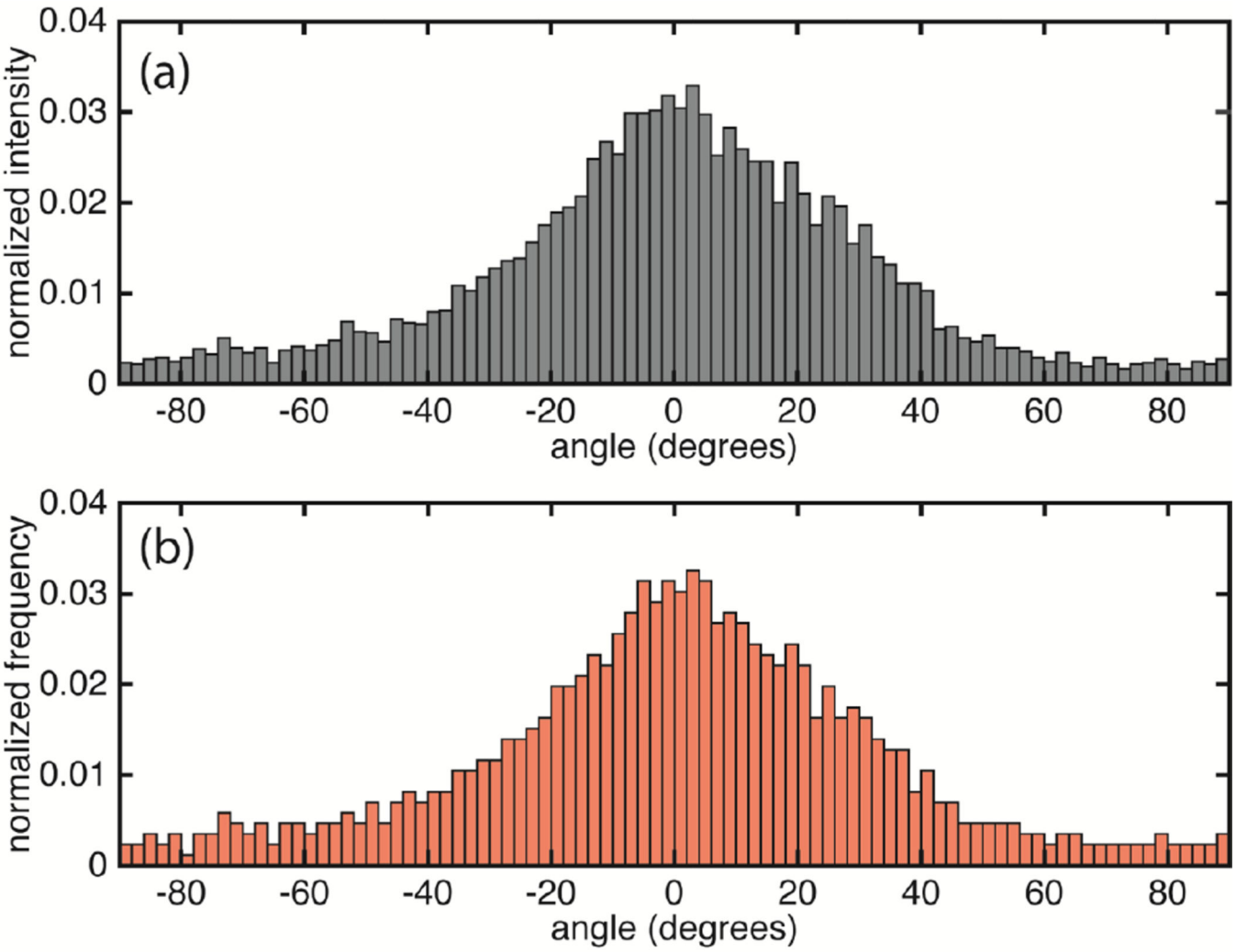

Figure 2.

(a) Orientation distribution for a representative collagen fiber network in the aortic media of BAV patient with aneurysm and that for the simulated network (NOI=0.56) (b). ODs have been normalized such that the sum of all frequencies equals 1. The CIRC direction is at 0 degrees while +/−90 degrees are along the LONG direction. The experimental OD is reproduced from (Phillippi et al., 2014). $p<0.01$ for the Chi-square test between the simulated and experimental orientation distribution.

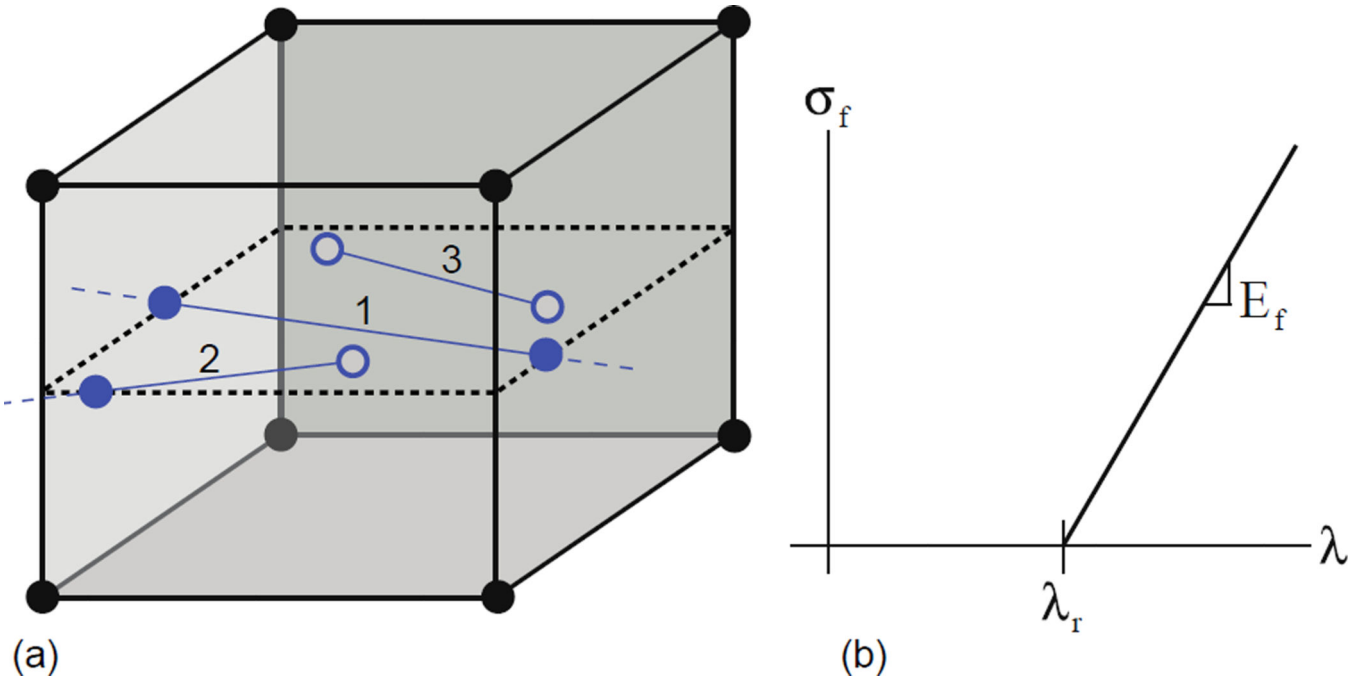

Figure 3.

(a) The fiber network is embedded within the volumetric element mesh, and they interact with the solid element through virtual nodes (solid and filled circles). The fibers can interact with the elements in three ways: 1) pass completely through the element, 2) partially pass through the element, or 3) lie entirely within the element. Solid circles are the endpoints of the fibers that lie on the boundary of the volumetric element while open circles lie within the volumetric element. The fibers are represented in the finite element formulation by their endpoints stored as virtual nodes defined by their isoparametric coordinates with respect to the element. For fiber nodes within the element, the endpoints are found directly. Endpoints on the boundary of the element are found through a line-plane intersection of the element face and the fiber. (b) The fiber material model is bilinear, with the fiber force zero until the recruitment stretch, λ_r, is reached. Slope of the linear curve beyond the recruitment stretch is the elastic modulus (E_f) for the fiber.

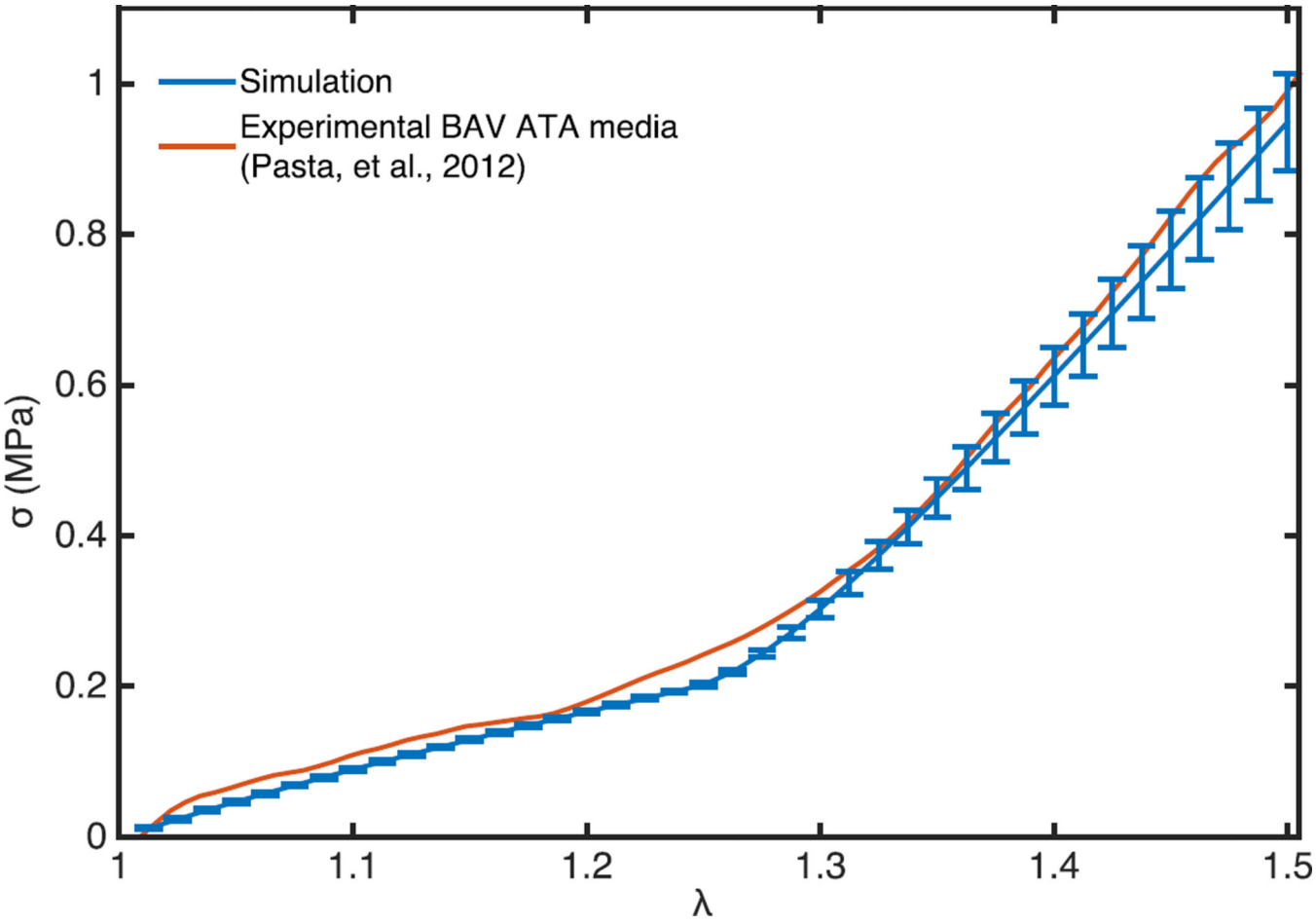

Figure 4.

The constitutive response of the simulated representative volume element and human BAV aneurysmic experimentally delaminated aortic media sample (from (Pasta et al., 2012)) is shown when loaded uniaxially in circumferential direction. The simulated curve shows the mean response of the five BAV aneurysmal networks. Bars show the standard deviation of the response. Goodness of fit ($R^2 = 0.996$) between the experimental and simulated response shows that the representative volume element is a suitable structural finite element model of the aortic media.

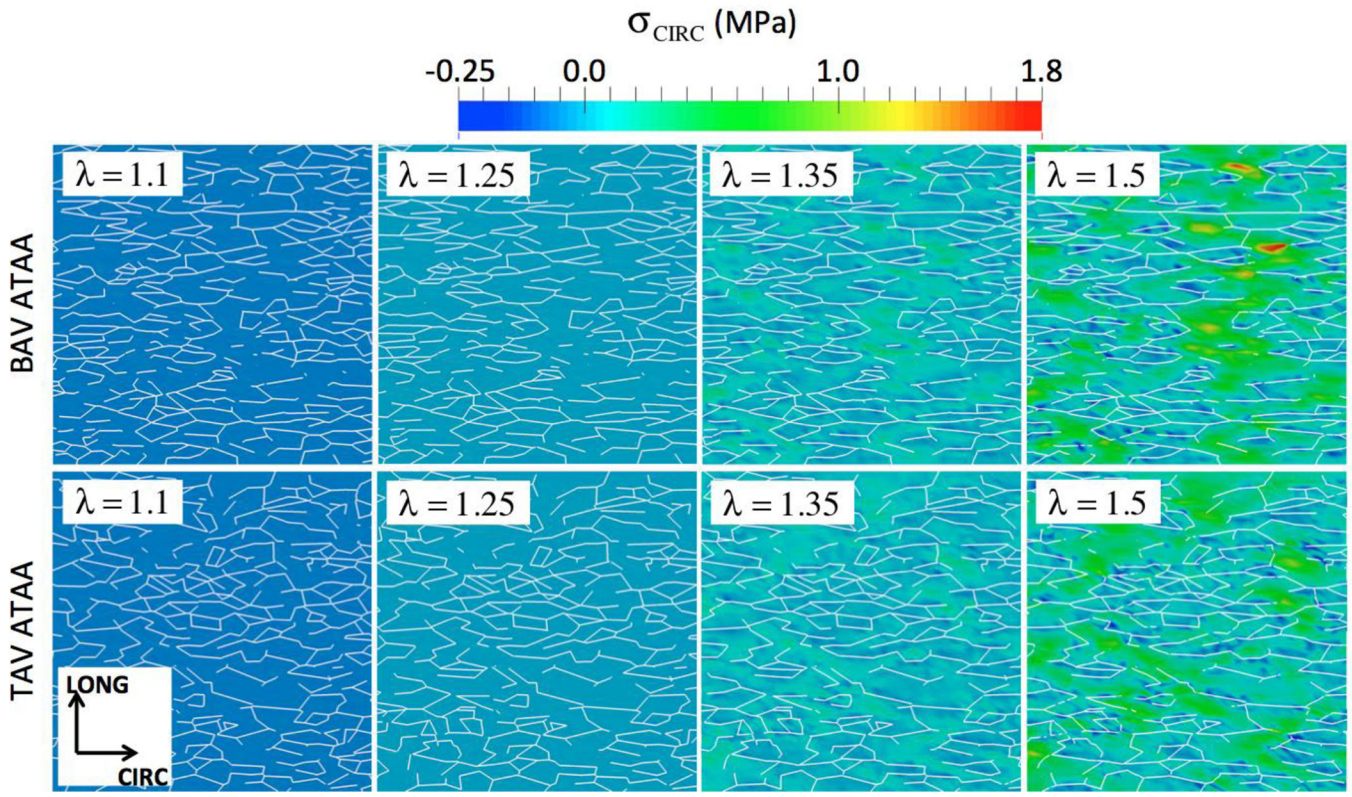

Figure 5.

Local variation of network density causes stress heterogeneity in the non-fibrous matrix stress. Contours for the CIRC component of the Cauchy stress tensor are shown on a 250 μm × 250 μm planar section centered in CIRC-LONG plane of the finite element model in the deformed configuration and just below the collagen fiber network at applied stretches of 1.1, 1.25, 1.35, and 1.5. Upper panels show the response from a representative BAV aneurysmal tissue (NOI=0.56) simulation and lower panels from a representative TAV aneurysmal tissue (NOI=0.23) simulation. White lines represent the location of collagen fiber segments. Matrix stresses are homogeneous until the fibers begin to take load, and can experience very high stress (red regions) at high applied stretch of 1.5.

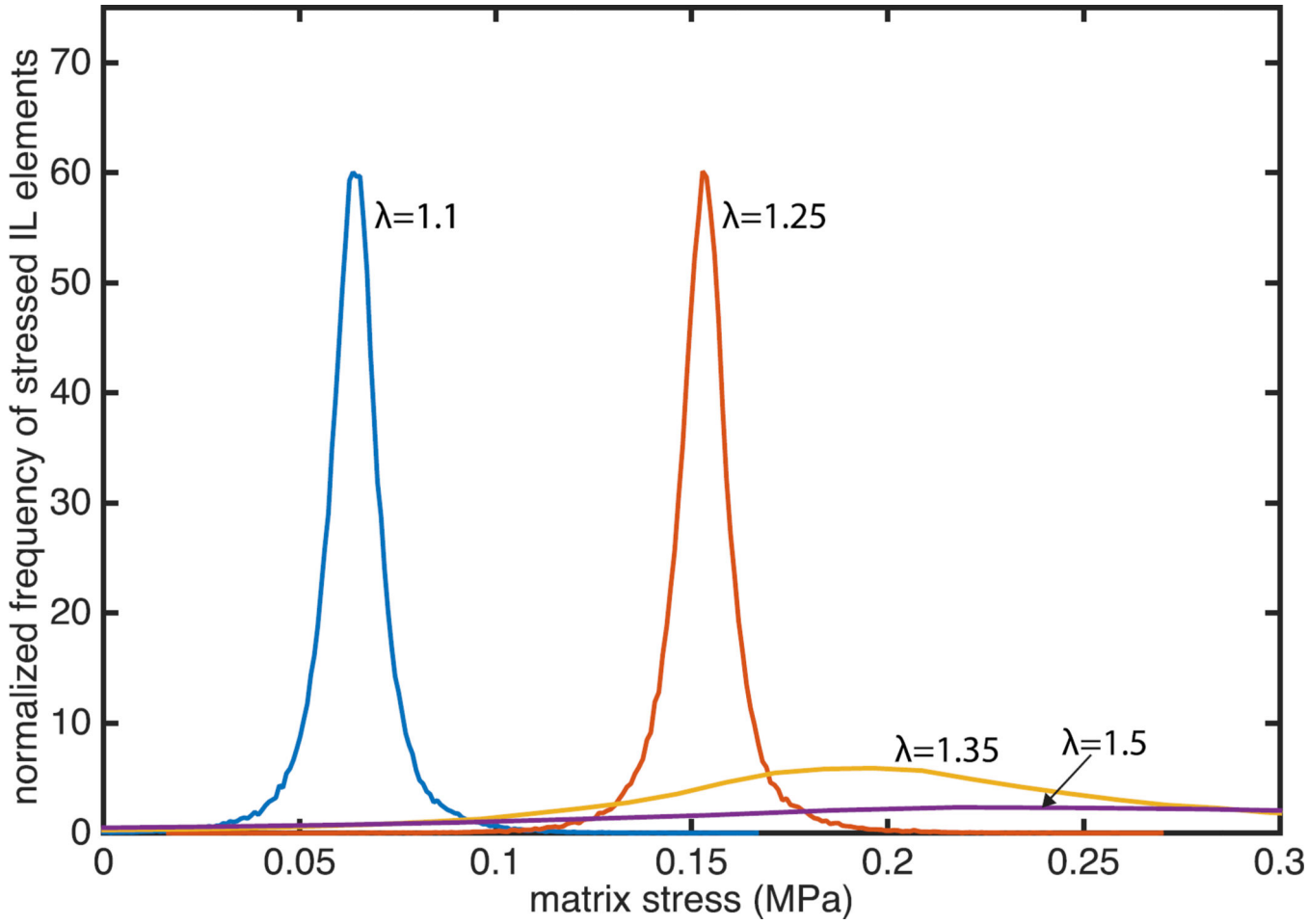

Figure 6.

Heterogeneity of the CIRC stresses in the finite elements of the interlaminar region increases with applied stretch. Stresses at each Gauss point in the interlaminar nonfibrous matrix for the representative BAV simulation (NOI=0.56) were collected at applied stretches of 1.1, 1.25, 1.35, and 1.5, and the resulting distributions are shown.

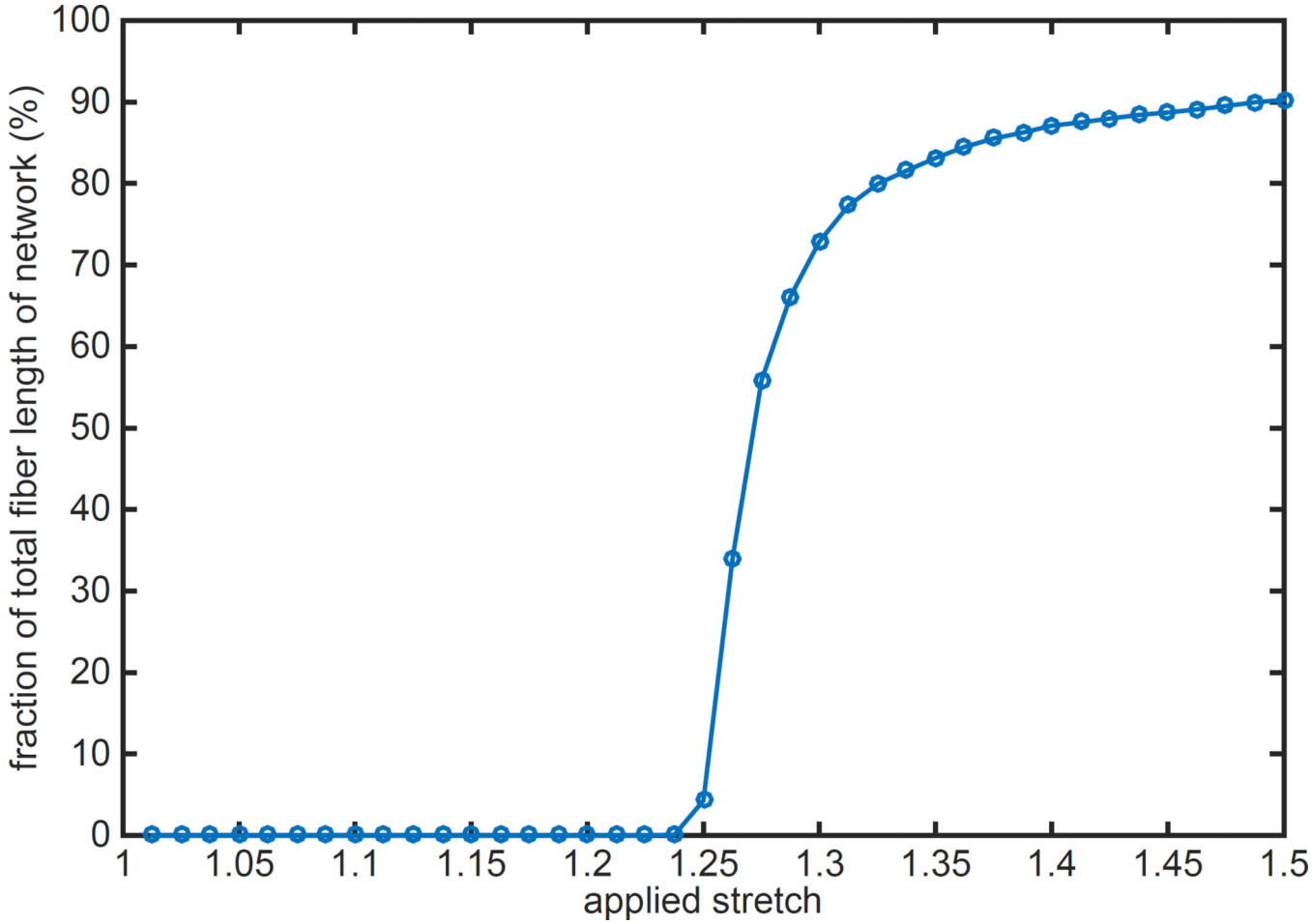

Figure 7.

Load bearing fibers as a percentage of total fiber length in the representative BAV ATA tissue model (NOI=0.56) against applied stretch are shown. No fiber bears load at low stretch while the load bearing fiber percentage saturates at high stretch. The transition occurs at a stretch of 1.25, the fiber recruitment stretch. Saturated value of load bearing fiber percentage at 90% signifies that about 10% of the total fiber length in the model never experiences any loading. This 10% is composed primarily of fibers orthogonal to the loading direction in the initial configuration. Recruitment rate and saturation values were not significantly different for the other simulations.

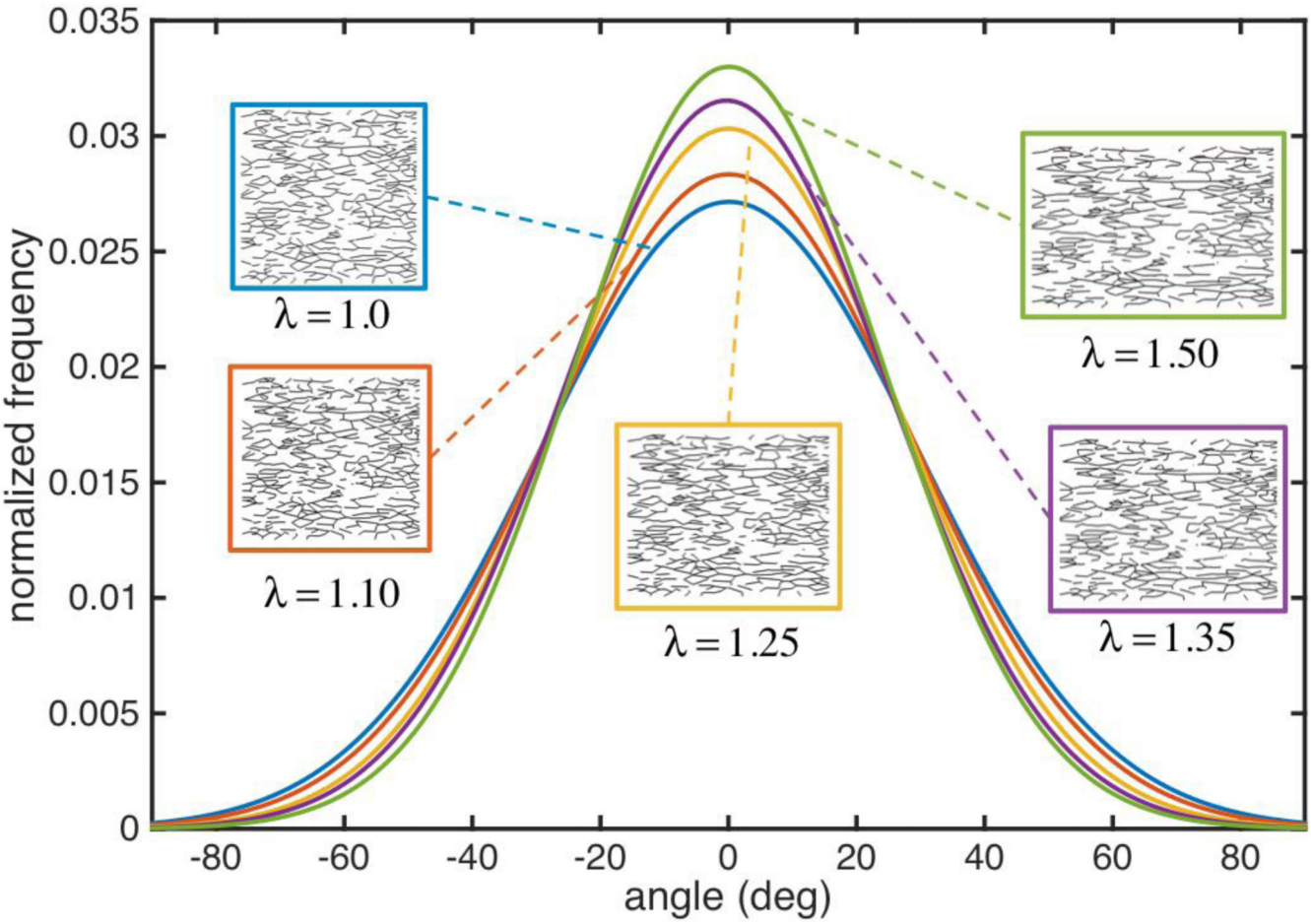

Figure 8.

The fiber OD for the representative BAV ATA tissue model (NOI=0.56) was constructed at five different applied stretch levels and are plotted after being fit to a normal distribution. The fiber network gradually aligns with the loading direction (0 degrees) as the applied stretch increases. Most of the alignment is seen with the fibers that were initial oriented along (and about) the loading direction. There is little difference in the orientation of fibers orthogonal to the loading direction (at the tails of the ODF curve). Actual fiber networks for each applied stretch are shown in inserts.

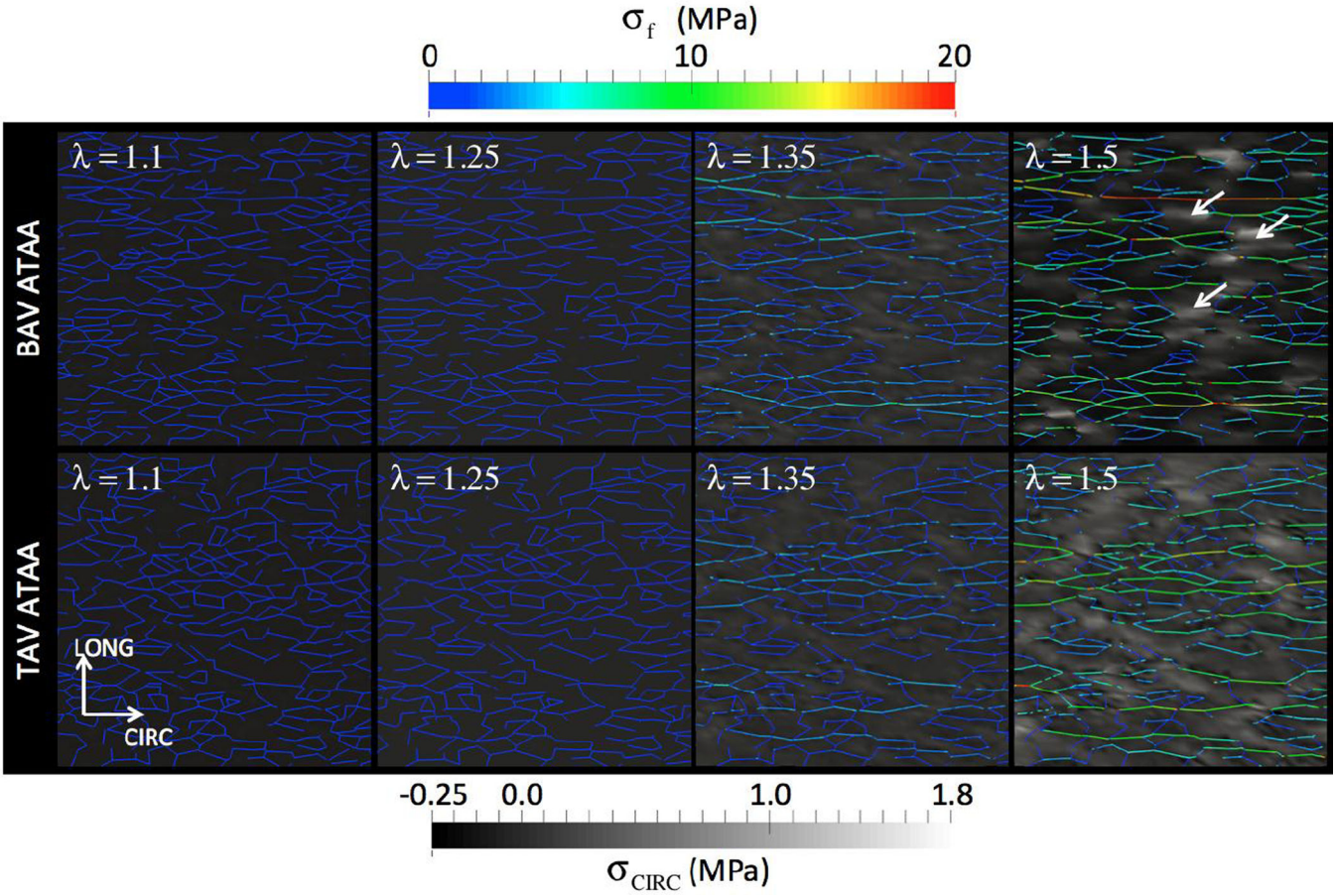

Figure 9.

Local variation of collagen fiber stress is plotted at different applied stretch. A 250 μm × 250 μm planar section of the fiber network centered in CIRC-LONG plane of the finite element model in the deformed configuration is shown in these figure at applied stretches of 1.1, 1.25, 1.35, and 1.5. Fibers initially along (and about) the loading direction (CIRC) became more aligned with applied stretch while the fibers predominately in the orthogonal direction remain unloaded. Fibers oriented in the CIRC direction take load soon after the applied stretch reaches the fiber recruitment stretch (1.25). White arrows show regions of high and low IL matrix stress region in the vicinity of the fibers. Matrix stress is shown in greyscale for comparison to Figure 5. Upper panels show the response from a representative BAV aneurysmal tissue (NOI=0.56) simulation and lower panels from a representative TAV aneurysmal tissue (NOI=0.23) simulation.

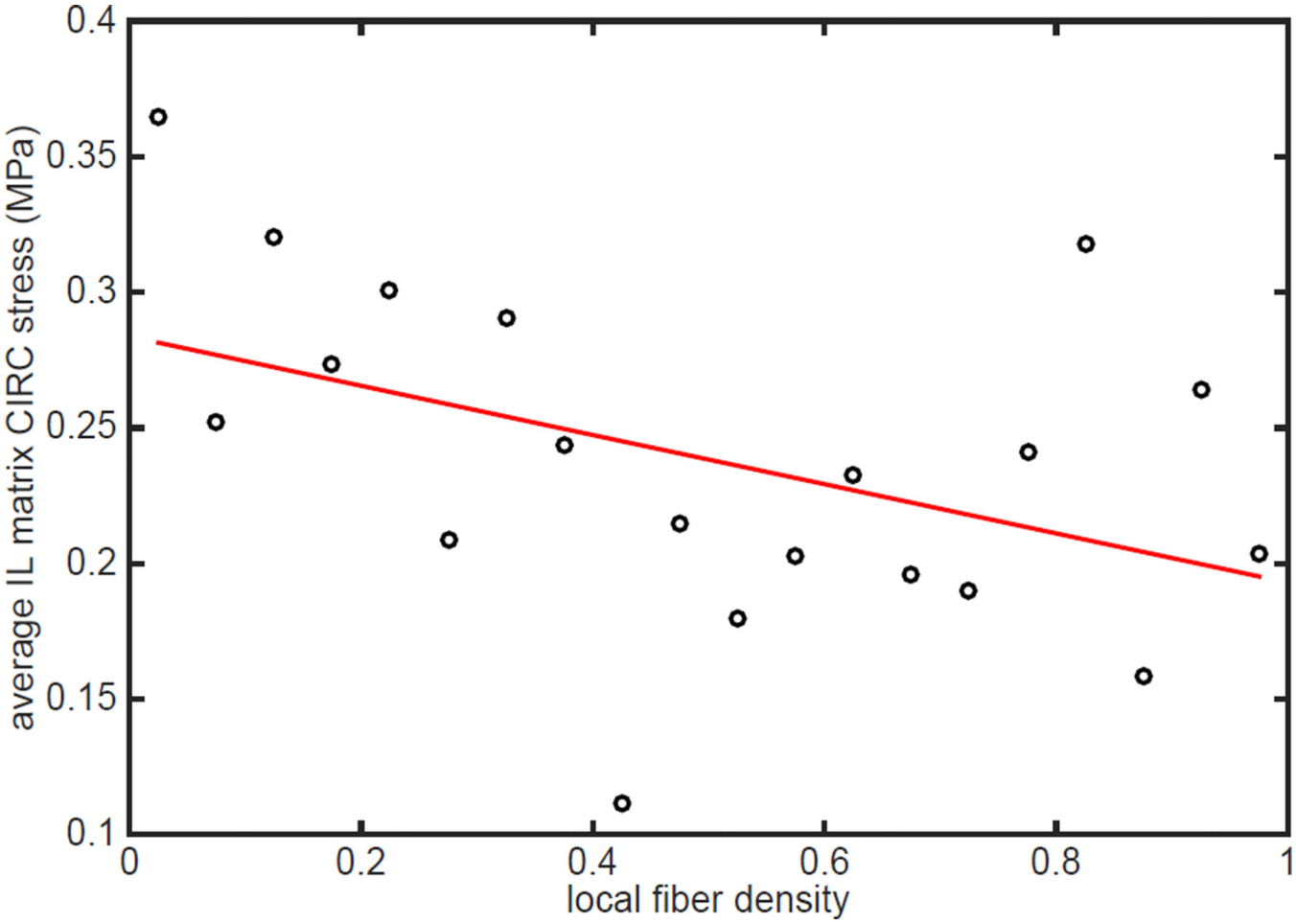

Figure 10.

Average stress in the interlaminar matrix of the representative BAV simulation (NOI=0.56) in the immediate vicinity of the fibers is shown with respect to local fiber density, expressed as the volume fraction of fibers. Fiber volume fraction and CIRC stress in all elements in the plane of the collagen network were collected at an applied stretch of 1.5. Elements were binned by volume fraction in 5% increments and the average stress of each bin was calculated. CIRC stress was negatively correlated with fiber density ($R=0.65$, $p<0.05$). Similar results were seen with the other BAV and TAV network simulations.

Table 1

Collagen network properties. The network was constructed based upon the experimental ODF. As many networks may share the same ODF, the SEN was compared against experimental data to ensure fidelity between the experimental and statistically equivalent networks.

Parameter	Experimental value (Koch et al., 2014)	Simulated value	Notes
Areal density	27–32%	34%	Input to simulated network
Intersection density	0.005–0.01 μm^{-2}	0.009 μm^{-2}	Input to simulated network
Average segment length	13–17 μm	9 μm	Derived from simulated network

Table 2

Fitted parameters for the models. The model parameters were modified until a good fit between the stress-stretch response of the experimental and simulated domain was achieved. One parameter of the non-collagenous matrix and two parameters of the collagen network were fitted. The elastin network properties were taken as fixed for the purpose of the fitting process.

Role	Parameter	Fitted value	Reported Value
Non-fibrous Matrix	μ_M	170 kPa	—
Collagen fiber	E_f	80 MPa	54 ± 25 MPa
	λ_r	1.25	1.2–1.4 (Zulliger and Stergiopulos, 2007)
Elastin fiber	E_f	3 MPa	1 MPa shear modulus (Fung, 1993)
	λ_r	1.0	